

Onset of internal transport barriers in tokamaks

L. A. Osorio

Instituto de Física, Universidade de São Paulo, São Paulo, SP 05315-970, Brazil

M. Roberto

*Departamento de Física, Instituto Tecnológico da Aeronáutica, São José dos Campos, SP 1228-900, Brazil**

I. L. Caldas

Instituto de Física, Universidade de São Paulo, São Paulo, SP 05315-970 - Brazil

R. L. Viana

Departamento de Física, Universidade Federal do Paraná, Curitiba, PR 81531-990, Brazil

Y. Elskens

*Aix-Marseille university, UMR 7345 CNRS, PIIM, campus Saint-Jérôme,
case 322, av. esc. Normandie-Niemen, 52, FR-13397 Marseille cedex 13, France*

Barriers have been identified in magnetically confined plasmas reducing the particle transport and improving the confinement. One of them, the primary shearless barriers are associated to extrema of non-monotonic plasma profiles. Previously, we identified these barriers in a model described by a map that allows the integration of charged particles motion in drift waves for a long time scale. In this work, we show how the existence of these robust barriers depends on the fluctuation amplitude and on the electric shear. Moreover, we also find control parameter intervals for which these primary barriers onset and break-up are recurrent. Another noticeable feature, in these transitions, is the appearance of a layer of particle trajectory stickiness after the shearless barrier break-up or before its onset. Besides the mentioned primary barriers, we also observe sequences of secondary shearless barriers, not reported before, created and destroyed by a sequence of bifurcations as the main control parameters, the fluctuation amplitude and electric shear, are varied. Furthermore, in these bifurcations, we also find hitherto unknown double and triple secondary shearless barriers which constitute a noticeable obstacle to the chaotic transport ^a.

arXiv:2108.11143v1 [physics.plasm-ph] 25 Aug 2021

^a This article has been accepted by the Journal Physics of Plasmas. It can be found at: <https://doi.org/10.1063/5.0056428>

* Author to whom correspondence may be addressed: r.marisa@gmail.com

I. INTRODUCTION

One of the questions of paramount importance in the quest for magnetically confined fusion plasmas is the understanding and control of radial particle transport [1–3]. In particular, in order to build a future tokamak-based fusion reactor, it is mandatory to improve the energy confinement by reducing particle transport to acceptable levels [4].

Auxiliary heating applied to tokamak discharges often leads to low confinement (L-mode) plasma regimes, for which there is an enhanced radial cross-field transport due to a high level of turbulence [5, 6]. By combining neutral beam heating and a divertor, it was possible to obtain a high confinement regime (H-mode) for tokamak plasmas, with reduced transport fluxes [7–9].

In the latter, there is a relatively high pedestal pressure profile in the plasma column, and a large pressure gradient at the plasma edge. This increased gradient is related to a local reduction of the turbulence levels due to $\mathbf{E} \times \mathbf{B}$ shear [10]. The edge transport barriers (ETBs) which are present in the H-mode can also exist inside the plasma core and are called generally internal transport barriers (ITBs), which are regions of reduced radial particle transport [2]. On both cases, the barriers are characterized by steep pressure gradients, however.

Another type of internal transport barrier has been recently proposed, the so-called shearless transport barriers (STBs), for which the pressure gradients are not necessarily high as in ITBs. The basic mechanism underlying the STBs is the existence of non-monotonic equilibrium radial profiles inside the tokamak. These profiles can be created by modifications of the plasma current profile and/or the application of radial electric fields [11].

An example of vanishing magnetic shear occurs for tokamak plasmas with a non-monotonic safety factor $q(r)$ profile, so that there can be one or more radial positions which are extremum points of $q(r)$ [12–14]. Particle transport is reduced for this type of non-monotonic discharges. At these points, a shearless toroidal magnetic surface is formed [15]. Given an external perturbation with modes resonant with the magnetic surfaces in both sides of the shearless torus, twin resonant island chains are formed therein, which produce a local region of chaotic magnetic field lines attached to the islands' boundaries [16, 17].

In a first approximation, plasma particles follow magnetic field lines which lie on magnetic surfaces, in such a way that there is no cross field transport. Within this picture, the tori surrounding the shearless curve act as dikes preventing chaotic transport. If we consider higher-order effects like finite Larmor-radius and collisions, there would be transport even in the presence of magnetic surfaces.

As the perturbation intensity increases, the width of these chaotic layers is also increased, engulfing other tori between the islands and the shearless torus. Increasing further the perturbation, all the tori can be destroyed and, even after the shearless torus is broken, it still acts as a transport barrier. This occurs because of a dynamical effect called stickiness, which makes a chaotic trajectory to wander erratically in the vicinity of the torus remnant, yielding trajectories with large escape times, so reducing effectively the transport fluxes [18].

There are other sources of vanishing shear that can be related to the formation of shearless transport barriers. The introduction of a bias electrode in the plasma column produces a radial electric field that improves plasma confinement in tokamaks [19]. In particular, a decrease was observed in the levels of the low-frequency component of the fluctuating floating potential as well as the turbulent-driven particle flux [20]. The production of shearless transport barriers due to a non-monotonic radial electric field produced by polarizing the tokamak vessel has been numerically investigated by considering a drift-kinetic model for particle transport driven by drift waves [21–23].

A further physical mechanism which can also trigger the formation of shearless transport barriers is the presence of non-monotonic plasma toroidal velocity profiles [24]. The existence of such barriers has been observed in the Texas Helimak, where a set of diagnostic probes is mounted to measure plasma flow velocity in various points, so that velocity shears can be detected in the discharges [25, 26].

We have applied the model introduced in [22] to predict numerically the existence of STBs in tokamak discharges with non-monotonic plasma profiles [21, 27, 28]. In this paper, our main goal is to examine in details the onset of shearless transport barriers in tokamaks associated to one of those described sources of non-monotonic plasma profiles, namely, the radial electric field. The common framework to deal with these physical mechanisms is the drift-kinetic model of Ref. [22], where we describe guiding center motion of plasma particles under $\mathbf{E} \times \mathbf{B}$ drift with contributions of the parallel velocity v_{\parallel} as well. The equations of motion are numerically integrated and Poincaré

maps are obtained for discrete times.

Since the ensuing dynamical model is non-integrable, we typically observe chaotic motion related to the resonant boundaries. From the numerically obtained Poincaré maps, we are able to detect the formation of shearless transport barriers. We call these barriers primary because they can be associated to the non-monotonic equilibrium profile and the corresponding extrema of the rotation number profile.

Using the drift-kinetic model, we investigate the behavior of the primary shear transport barriers when model parameters are changed, particularly how they depend on the amplitude of electrostatic fluctuations and the extremum of radial electric field. We show that the barriers break up and resurge, recurrently, as those parameters are varied. In these transitions, after the shearless barrier break-up or before its onset, we also find the appearance of a layer of particle trajectory stickiness, which is a obstruction to chaotic transport.

Besides the mentioned primary barriers, we also find secondary shearless barriers recurrently created and destroyed by a sequence of bifurcations that creates new extrema in the rotation number profile. Furthermore, in these bifurcations, we also find hitherto unknown double and triple secondary shearless barriers which also constitute a noticeable obstacle to the chaotic transport.

The paper is organized as follows: Section II introduces the drift-kinetic model and the non-monotonic plasma profiles used in numerical simulations. Section III discusses the influence of the fluctuation amplitude on the shearless transport barriers. The formation of effective barriers due to stickiness effect, after the shearless curve has been destroyed, is discussed in Section IV. The influence of the radial electric field profile on the formation of shearless barriers is the subject of Section V. The last Section is devoted to our Conclusions.

II. DRIFT WAVE MODEL

The chosen drift wave model introduces the basic equations of motion to describe the trajectories of particles along magnetic field lines and electrical drifts. We consider an electrostatic equilibrium field in the radial direction and drift waves that propagate in the poloidal and toroidal directions. These drift waves arise from non-uniformity at the plasma edge and are analyzed in the toroidal section of magnetic confinement in the tokamak [1, 22, 27–30]. Fluctuations in electrostatic potential are written as a function of amplitude, and in spatial and temporal modes [27, 28].

The trajectories of the particles are described by the movement of the guiding center

$$\frac{d\mathbf{x}}{dt} = v_{\parallel} \frac{\mathbf{B}}{B} + \frac{\mathbf{E} \times \mathbf{B}}{B^2} \quad (1)$$

We consider, initially, that the components of this equation are given in local polar coordinates $\mathbf{x} = (r, \theta, \varphi)$.

This plasma configuration corresponds to a cylindrical approximation of a toroidal section of a tokamak of high aspect ratio ($a/R \simeq 0.3$), where a and R are, respectively, the minor and major plasma radius. For the field components, we assume a magnetic configuration with $B \approx B_{\varphi} \gg B_{\theta}$ and the safety factor given by $q(r) = \frac{rB_{\varphi}}{RB_{\theta}}$. The electric field consists of an equilibrium part with intensity given by E_r , defined by a radial profile, and a floating part, so that $\tilde{\mathbf{E}} = -\nabla\tilde{\phi}$. Therefore, this model allows to investigate the simultaneous influence of the electric shear, due to the spatial variations of the electric field, and the magnetic shear, when considering the spatial variations of the safety factor, in the chaotic transport at the plasma edge.

We follow the procedure adopted in reference [22], writing the equations in the action variable $I \equiv (r/a)^2$ and angle variable $\psi \equiv M\theta - L\varphi$. Poloidal and toroidal spatial modes are defined, respectively, by the wave numbers M and L . In this way we assume coherent oscillations, where ψ represents a helical angle defined by dominant modes. When considering these new variable components of the guiding center, we obtain

$$\frac{dI}{dt} = 2M \sum_n \phi_n \sin(\psi - n\omega_0 t + \alpha_n) \quad (2)$$

$$\frac{d\psi}{dt} = \frac{a}{R} v_{\parallel}(I) \frac{[M - Lq(I)]}{q(I)} - \frac{M}{\sqrt{I}} E_r(I) \quad (3)$$

where a normalization with the characteristic magnitude scales a , B and E_0 was done. Note that all the plasma profiles are defined as functions of the action variable. For the floating potential, we use a finite mode drift wave spectrum,

$$\tilde{\phi}(\mathbf{r}, t) = \sum_n \phi_n \cos(\psi - n\omega_0 t + \alpha_n) \quad (4)$$

where ϕ_n is the perturbed amplitude, ω_0 is the lowest angular frequency of the drift wave spectrum and α_n are constant phases that do not affect the resonant conditions. Temporal modes are defined by the wave numbers n . Thus, we can assume one or more drift waves that describe fluctuations in the electrostatic potential of the model.

In the next sections, for numerical applications, we introduce typical parallel speed and radial electric field profiles experimentally measured in the TCABR tokamak [30]. We also assume a monotonic safety factor profile commonly observed in tokamaks [4]. The resonance conditions are determined by the combination of the safety factor, parallel plasma velocity and electric field profiles. Thus, taking $\frac{d}{dt}(\psi - n\omega_0 t - \alpha_n) = 0$, we obtain the primary resonance condition. Furthermore, we also show the Poincaré maps by integrating the equations (2) and (3) for various initial conditions chosen to clearly represent the most important islands, invariant lines and the chaotic region. The intersections of the integrated trajectories are selected at the toroidal section corresponding to instants $t_j = j 2\pi/\omega_0$ ($j = 0, 1, 2, \dots$). In Poincaré maps, the minor plasma radius lies at $I = 1.0$, but we consider I up to 1.4 to investigate the particle transport to the chamber wall.

III. INFLUENCE OF THE FLUCTUATION AMPLITUDE ON THE SHEARLESS TRANSPORT BARRIERS

According to equation (2), for null perturbing amplitudes, $\phi_n = 0$, the system is integrable, it means that each trajectory is periodic or quasi-periodic and stays in invariant lines in the Poincaré map, with the initial action $I_0 = \text{constant}$. When $\phi_n \neq 0$, we have chaotic trajectories and regular invariant lines and we can use the rotation number, defined as $\Omega = \lim_{i \rightarrow \infty} (\psi_i - \psi_0)/i$, where ψ_i refers to the i -th section, to analyze the behavior of the invariant lines in the phase space. The rotation number profile is determined for initial conditions with a fixed angle ψ_0 for several values of action variable I . Although other choices of ψ_0 would result in different profiles, the identified islands and other invariants would be essentially the same. This happens because each invariant and island depend on both variables ψ and I , but are labeled by a unique identifying rotation number. If $d\Omega/dI = 0$, the profile has an extremum at (I, ψ_0) . This point is part of a shearless invariant curve, which acts as a barrier separating the particle orbits in the phase space and reducing the particle transport. These are the primary shearless invariant curves if their origin can be associated to the rotation number extrema obtained from the equilibrium plasma profiles. However, in this work we also present secondary shearless invariant curves that are due to bifurcations that create new rotation number extrema for varying control parameters.

In order to solve our numerical model, we use the parallel velocity and radial electric field profiles, with $a = 0.18\text{m}$, $B = 1.1\text{T}$ and $E_0 = 4.6\text{kV/m}$, as given in reference [21], which are similar to those observed in TCABR tokamak [30]. The velocity profile is given by equation (5), which fits with experimental TCABR data points as described in reference [21]. The equilibrium radial field E_r is written in equation (6), with $\alpha = -0.563$, $\beta = 1.250$ and $\gamma = -1.304$. Furthermore, we assume the safety factor profile as equation (7), a common approximation for large aspect ratio tokamaks.

$$v_{\parallel}(r) = -1.43 + 2.82 \tanh\left(20.3 \frac{r}{a} - 16.42\right) \quad (5)$$

$$E_r(r) = 3\alpha \left(\frac{r}{a}\right)^2 + 2\beta \frac{r}{a} + \gamma \quad (6)$$

$$q(r) = 1.0 + 3.0 \left(\frac{r}{a}\right)^2 \quad (7)$$

Applying the resonant condition for the chosen radial profiles, we verify that the resonant modes are $n = 3$ and $n = 4$. We select from the spectrum analysis a frequency around 62.1kHz, which gives $\omega_0 = 2.673$. The perturbing

electric potential amplitudes ϕ_n are normalized by aE_0 . We consider spatial wave numbers $M = 16$ and $L = 4$, chosen as typical numbers in the tokamak wave spectrum at plasma edge [22].

In order to analyze the influence of the fluctuation amplitudes on the shearless barriers, we keep fixed the perturbation amplitudes $\phi_3 = 1.0 \times 10^{-3}$ and $\phi_4 = 0.12 \times 10^{-3}$ and vary the non-resonant mode ϕ_2 . We keep constant all the parameters of the equilibrium profiles. The objective is to investigate the recurrent break-up and onset of the barriers as the fluctuation amplitude is varied. Following that, Figure 1 shows the Poincaré maps for $\phi_2 = 0, 1.5 \times 10^{-3}, 1.6 \times 10^{-3}$ and 1.8×10^{-3} . The barrier already exists for a null $n = 2$ amplitude, breaks up for the perturbing amplitude $\phi_2 = 1.6 \times 10^{-3}$ and resurges for $\phi_2 = 1.8 \times 10^{-3}$. So we see that the existence of the barrier is sensitive to small variations in the fluctuation amplitude, a characteristic that will be explored in this section.

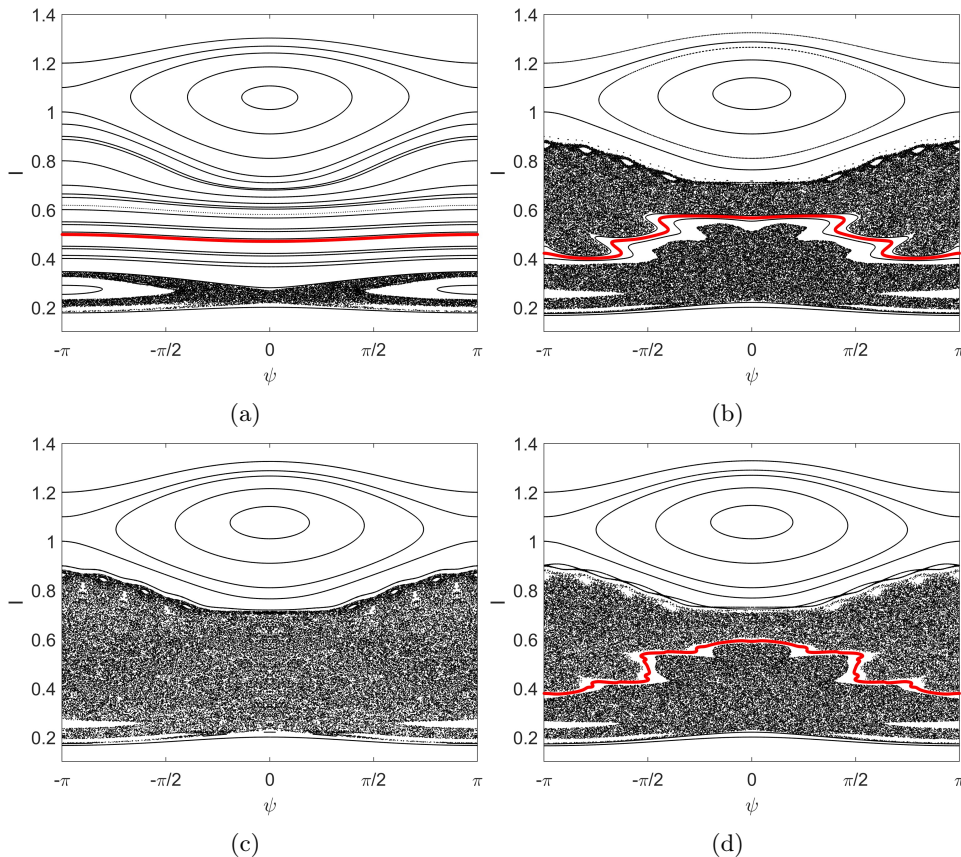


Figure 1: Poincaré maps for (a) $\phi_2 = 0$, (b) $\phi_2 = 1.5 \times 10^{-3}$, (c) 1.6×10^{-3} and (d) 1.8×10^{-3} . The shearless curve, marked in red, disappears for $\phi_2 = 1.6 \times 10^{-3}$ and resurges for $\phi_2 = 1.8 \times 10^{-3}$.

To confirm the existence of the shearless curve we present, in Figure 2, the magnified rotation number profiles for Figures 1b and 1d, calculated for initial conditions at $\psi = 0$, with local I maxima. The I maxima and the angle $\psi = 0$ are used as initial coordinates and iterated to trace in red the shearless curves shown in Figures 1b and 1d.

Next, for increasing values of ϕ_2 we observe a sequence of shearless curve break-ups in phase space. Figure 3 shows three shearless curves for $\phi_2 = 6.8 \times 10^{-3}$, two shearless curves for $\phi_2 = 6.9 \times 10^{-3}$, one shearless curve for $\phi_2 = 7.1 \times 10^{-3}$ and no shearless curve for $\phi_2 = 7.5 \times 10^{-3}$ with a stickiness region left by the previous barrier. This kind of bifurcation has been observed in theoretical non-twist dynamical systems [31] and, in the context of this article, represents a reinforcement of barriers attenuating the particle transport.

For each coloured STB seen in Figure 3, we present, in Figure 4, the associated magnified rotation number profiles in the same color as the STB curves, calculated in the non chaotic map region, for initial conditions with $\psi = 0$. These STBs can be generated by the initial coordinates $\psi = 0$ and I corresponding to the local maxima indicated in the profiles of Figure 4.

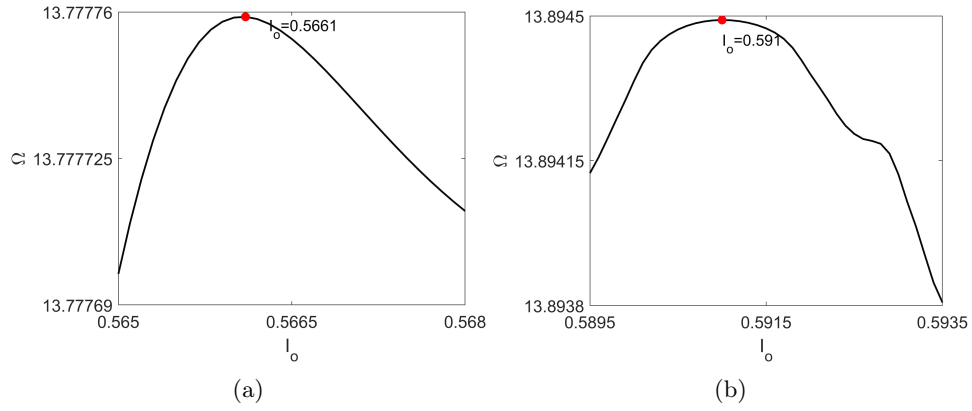


Figure 2: Rotation number profiles to (a) $\phi_2 = 1.5 \times 10^{-3}$ and (b) 1.8×10^{-3} for a set of initial conditions I_0 . The red dots correspond to shearless actions, indicated in the figures, required to obtain the shearless curves of Figures 1b and 1d.

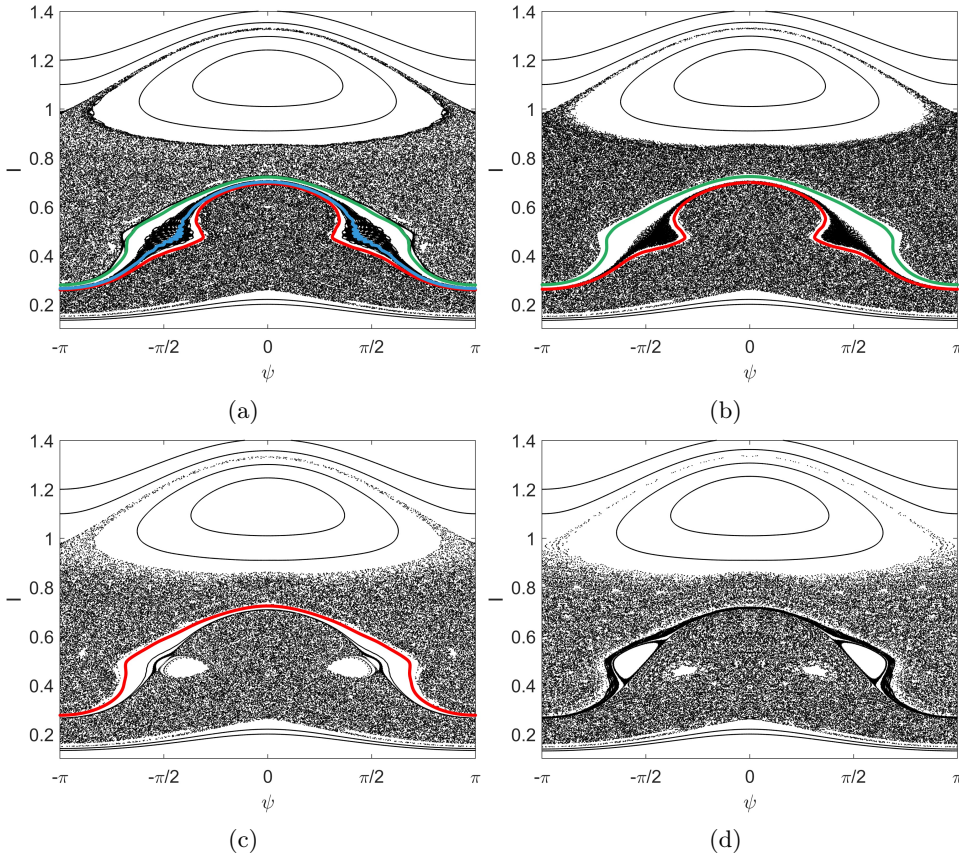


Figure 3: Three shearless curves, marked in red, blue and green, for (a) $\phi_2 = 6.8 \times 10^{-3}$. (b) Break-up of a shearless curve, with two remaining shearless curves, marked in red and green, for $\phi_2 = 6.9 \times 10^{-3}$. (c) One remaining shearless curve, marked in red, for $\phi_2 = 7.1 \times 10^{-3}$. (d) No shearless curve, for $\phi_2 = 7.5 \times 10^{-3}$.

To show that the existence of barriers depends on the fluctuation amplitude ϕ_2 , we check their existence in an interval of ϕ_2 from 0 to 8.5×10^{-3} , with a step 0.1×10^{-3} . The results are shown in Figure 5. In this figure, the red, blue and green bars represent the amplitude range for which barriers exist, otherwise we draw a black bar, when the barrier is not observed. We also present magnifications to better show the shearless bifurcations changing the

number of barriers. Figure 5a shows the rotation number as a function of fluctuation amplitude and Figure 5b shows the shearless barrier position as a function of ϕ_2 . We conclude that, as the amplitude of the fluctuation varies, the shearless barriers can be recurrently destroyed and restored. It means that the existence of barriers, in tokamak discharges, may depend on the fluctuation amplitude. In addition, for some fluctuation ranges, there are barrier bifurcations giving rise to a second and, possibly, a third barrier.

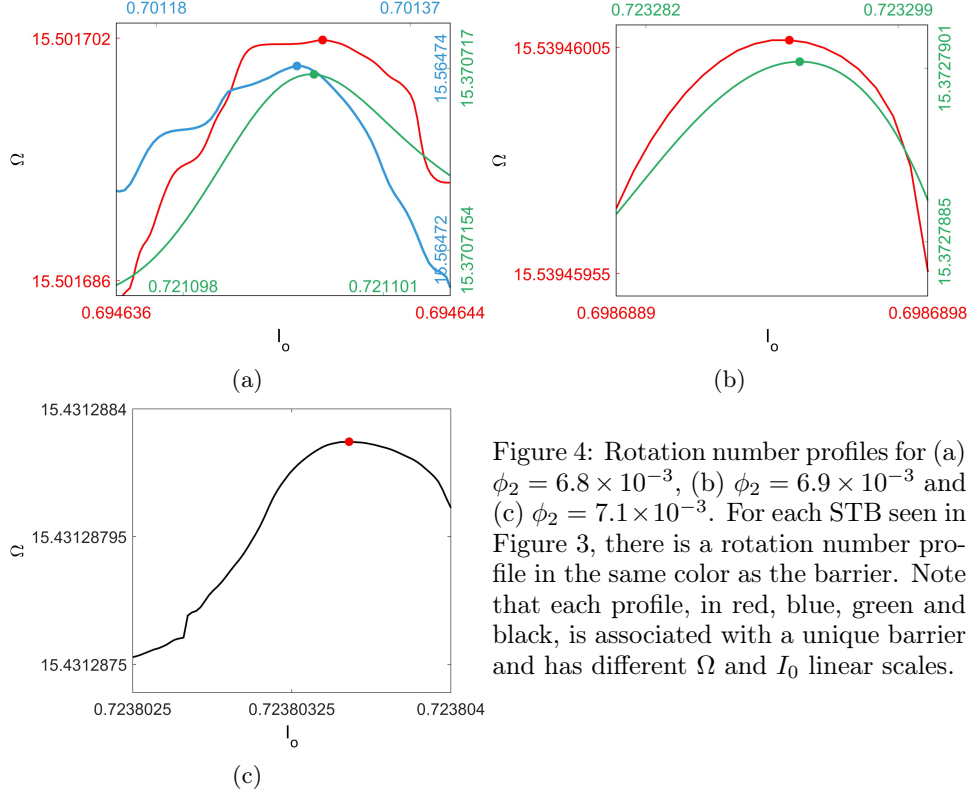


Figure 4: Rotation number profiles for (a) $\phi_2 = 6.8 \times 10^{-3}$, (b) $\phi_2 = 6.9 \times 10^{-3}$ and (c) $\phi_2 = 7.1 \times 10^{-3}$. For each STB seen in Figure 3, there is a rotation number profile in the same color as the barrier. Note that each profile, in red, blue, green and black, is associated with a unique barrier and has different Ω and I_0 linear scales.

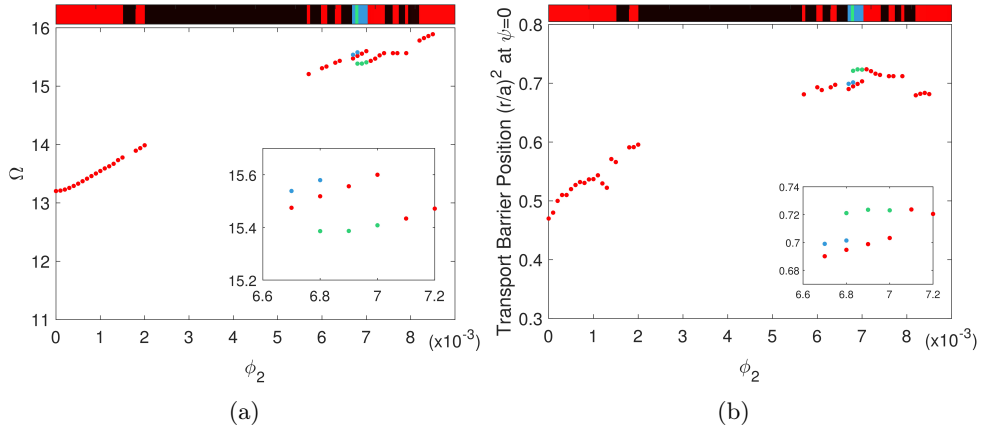


Figure 5: (a) Rotation number Ω as function of the fluctuation amplitude ϕ_2 . Red (black) bars indicate the existence (non existence) of shearless barriers. For some values of ϕ_2 , there are two or three shearless curves, indicated in blue or green bars. (b) Transport barrier position I at $\psi = 0$ versus ϕ_2 .

IV. PERSISTENT BARRIERS

A noticeable feature in non-twist systems is the appearance of a layer of stickiness after the shearless barrier break-up or before its onset [32]. A stickiness layer separates the chaotic region in two parts and, to cross this layer,

orbits get trapped for a high number of iterations [33]. Accordingly, for some domains of the amplitude perturbation, in the present analysis we observe that stickiness regions appear in phase space, associated to the shearless barrier break-up or to its onset. This is the case for $\phi_2 = 2.0 \times 10^{-3}$. Taking $\phi_2 = 2.1 \times 10^{-3}$, the barrier is destroyed and a stickiness region is magnified, as shown in Figure 6, separating the chaotic orbits around the stickiness layer.

In Figure 6b, one chaotic orbit in blue and another one in black fill separated areas in phase space, with a high concentration of iterations in the stickiness region, spending a long time to cross this region. The possible crossings are too long to be observed in Figure 6b. Thus, even if the barrier is broken up, there is a long stickiness inhibiting the particle transport in this region indicating the persistence of barrier effect, even after the barrier disappearance.

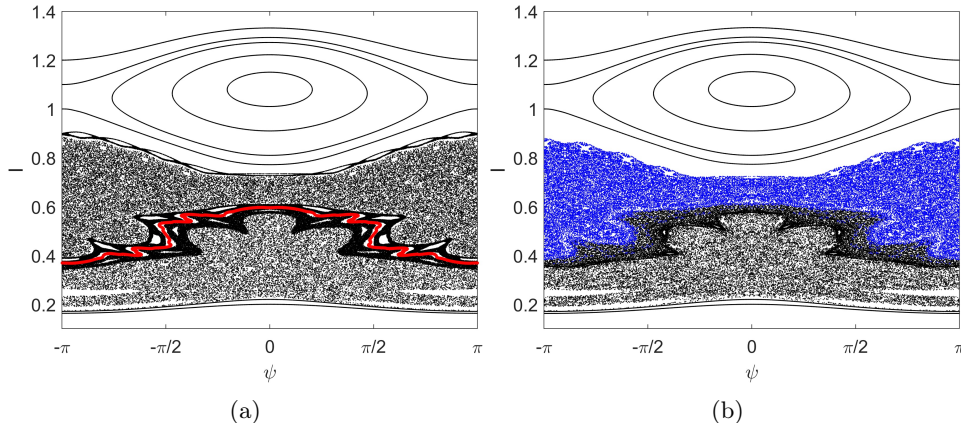


Figure 6: (a) Shearless curve, in red color, for $\phi_2 = 2.0 \times 10^{-3}$ and the stickiness appearance around this curve. (b) For $\phi_2 = 2.1 \times 10^{-3}$, the shearless curve is destroyed and stickiness region expanded. Two chaotic orbits in blue and black are concentrated in the stickiness region and take a long time to cross this region. The stickiness regions are identified by the high concentration of black points.

Figure 7 shows the emergence of stickiness, precursor of the shearless curve, for $\phi_2 = 5.6 \times 10^{-3}$. For $\phi_2 = 5.7 \times 10^{-3}$, the shearless curve onset occurs in the stickiness layer. This transformation is the reverse sequence of that shown in Figure 6, namely, the stickiness appears before the barrier onset and not after its destruction. It also indicates the persistence of the barrier effect after this disappearance for decreasing fluctuation amplitude.

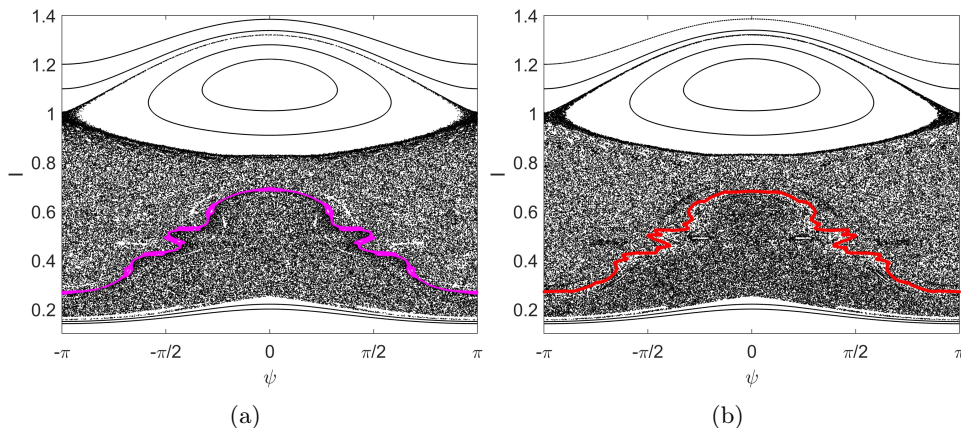


Figure 7: (a) Emergence of stickiness, precursor of the shearless curve for $\phi_2 = 5.6 \times 10^{-3}$. The stickiness layer is represented in magenta, where the shearless curve is created. (b) Shearless curve onset in the stickiness region, for $\phi_2 = 5.7 \times 10^{-3}$, in red.

As we show in Figure 8, increasing the perturbation amplitude, for $\phi_2 = 6.6 \times 10^{-3}$, there is no shearless curve. However, for $\phi_2 = 6.61 \times 10^{-3}$ a shearless curve appears and then, for $\phi_2 = 6.7 \times 10^{-3}$, we see two shearless curves (in blue and red). In this Figure, we have an example of a large region of stickiness, with many visible islands, associated to the onset of multiple shearless barriers.

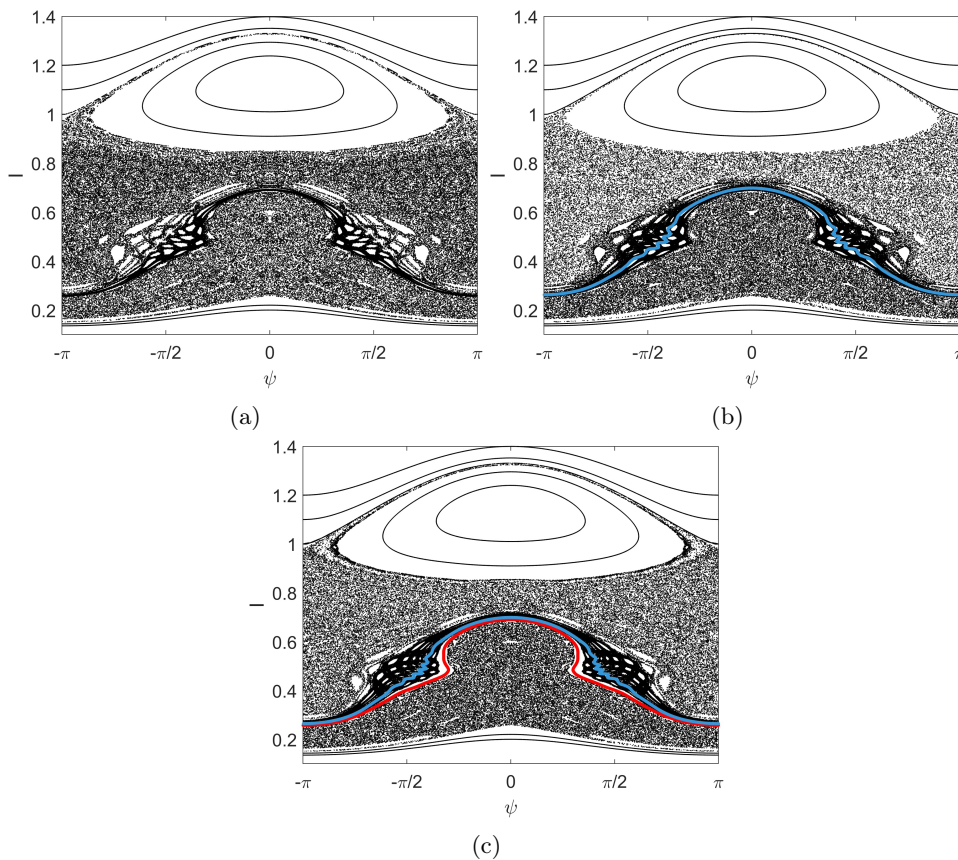


Figure 8: (a) No shearless curve for $\phi_2 = 6.6 \times 10^{-3}$. (b) Emerging shearless curve for $\phi_2 = 6.61 \times 10^{-3}$, in blue color. (c) Two shearless barriers for $\phi_2 = 6.7 \times 10^{-3}$, in red and blue.

V. INFLUENCE OF THE RADIAL ELECTRIC FIELD PROFILE ON THE SHEARLESS TRANSPORT BARRIERS

The experiments show that the transport barriers appear by modifications of the radial electric field E_r in high confinement regime, as discussed in the Introduction. On the other hand, shearless barriers appear as a mechanism to prevent chaotic particle transport: even after the invariant curve has been broken, the islands still remain with large stickiness that reduce the transport.

To verify the influence of the radial electric field profile on the existence of the shearless barriers, we fix the fluctuation amplitude ϕ_2 , choosing $\phi_2 = 1.6 \times 10^{-3}$, and vary the parameter k , defined as $k = -\beta/(3\alpha)$, that corresponds to the radial position of the maximum of the electric field (normalized to the plasma radius). The parameters α and β are defined in the expression of E_r introduced in equation (6) [21]. In Sections III and IV, $k = 0.74$. Figures 9a and b show how the rotation number changes with the parameter k . In this figure, the red and blue bars indicate the parameter range for which barriers are identified and the black bars represent the barriers absence. Figure 9b is a magnification of Figure 9a. As the radial electric field profile changes, the resonance condition also changes and this is the reason why there is no shearless barrier in the range around $k = 0.74$, where the resonance condition also includes $n = 2$. Figure 9 also shows an interval of parameter k for which two barriers exist.

It is also noted that in the interval $k = [0.7, 0.78]$, as shown in the top bar of Figure 9b, the shearless barrier appears and disappears on repeated occasions. To clarify this point, we show in Figure 10a the Poincaré map for $k = 0.704$. There is no shearless barrier in this case, only the chaotic trajectories are observed. A small modification of parameter k to $k = 0.7044$, as shown in Figure 10b, determines the appearance of the shearless barrier and this scenario occurs repeatedly as the electric field profile changes, as shown in Figures 9a and 9b.

Figures 11a and b show the transport barrier position I , at $\psi = 0$, as a function of k for a fixed amplitude

$\phi_2 = 1.6 \times 10^{-3}$. Figure 11b is a magnification of Figure 11a. Similarly to the conclusions of Figure 9, on varying the parameter k we find that the shearless barriers are sensitive to this parameter. Thus, a small variation of k , inherent to the plasma discharges evolution, can break or create such barriers or even move it towards the edge.

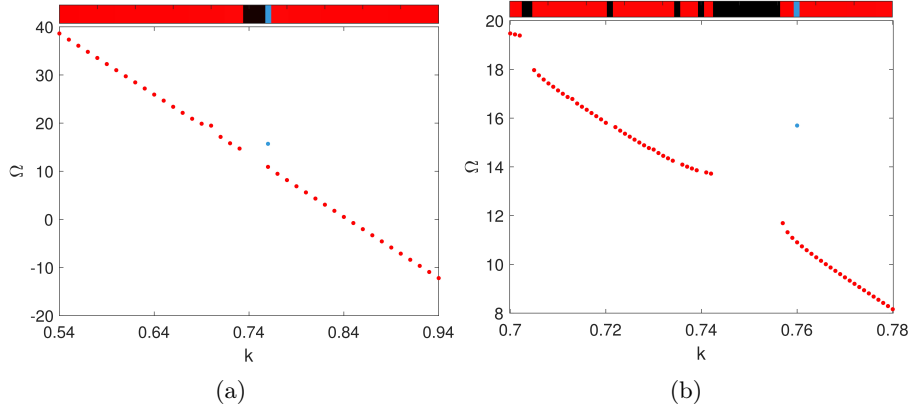


Figure 9: Rotation number Ω as function of the parameter k . Red (black) bars indicate the existence (non existence) of shearless barriers. The blue bar indicates a interval with two shearless barriers. (a) Ω versus k for fixed $\phi_2 = 1.6 \times 10^{-3}$. (b) Zoom in the interval $0.7 \leq k \leq 0.78$.

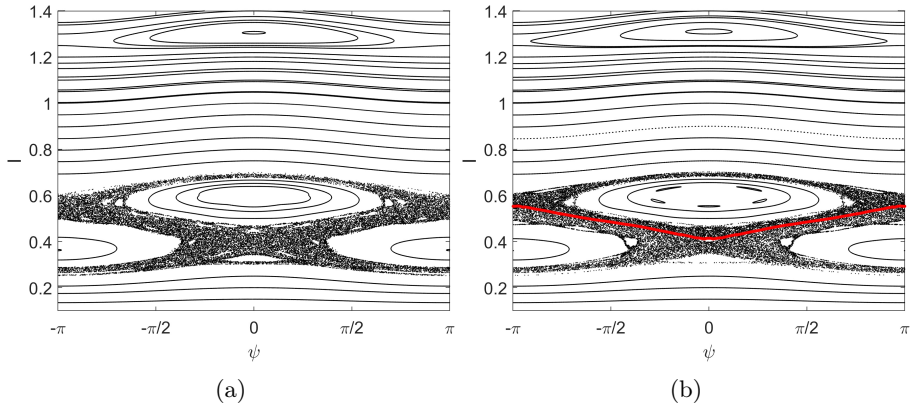


Figure 10: (a) No shearless barrier for $k=0.704$ and (b) sudden appearance of a shearless barrier around $k=0.7044$, marked in red.

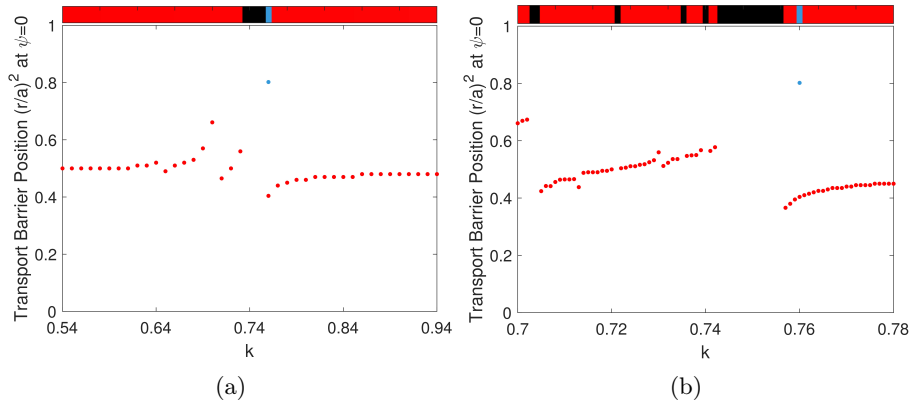


Figure 11: (a) Transport barrier position I , at $\psi = 0$, versus k for a fixed $\phi_2 = 1.6 \times 10^{-3}$. (b) Zoom in the interval $0.7 \leq k \leq 0.78$.

VI. CONCLUSIONS

The existence of shearless transport barriers represents a novel feature in the investigation of the possible ways to control or mitigate particle transport in tokamaks and other toroidal devices like the Texas Helimak. While internal transport barriers are usually related to strong density gradients, both in the plasma edge as well as its core, shearless transport barriers appear due to a different cause, namely the existence of non-monotonic plasma profiles. These primary shearless barriers are located at the extremum points of those profiles, and do not need strong density gradients to be effective against particle transport.

There are three types of non-monotonic plasma profiles which can be harnessed in order to create shearless transport barriers: (i) magnetic shear (safety factor); (ii) radial electric field; and (iii) toroidal plasma velocity. In the present paper, we investigated the production of shearless transport barriers through the non-monotonic profile (ii), using a drift-kinetic model (the safety factor profile was kept monotonic). The numerical integration of the model equations is used to obtain a Poincaré map for canonically conjugate variables (I, ψ) .

Considering that the chaotic particle transport is influenced by a turbulent fluctuation spectrum, we considered a finite drift-wave mode spectrum for the floating electrostatic potential. The intensity of the non-resonant mode (ϕ_2) has been used as a variable control parameter. On increasing the latter, we have shown that a primary shearless transport barrier which is destroyed for a given value of ϕ_2 can reappear at a slightly larger value. The reason for this behavior is that shearless barriers occur at local extremum points of the rotation number, which is the average progress of the ψ variable per map iteration. Alterations in the value of the perturbation strength modify the rotation number radial profiles, what can either create or destroy local extrema. Moreover, for some specific intervals of the control parameters, we identify new sequences of secondary transport barriers not associated to the non-monotonic plasma profile. Furthermore, these secondary barriers are formed by two or three coexisting shearless invariants, constituting a noticeable obstacle to the chaotic particle transport at the plasma edge.

The shearless barriers described above are truly invariant curves of the Poincaré map of the particle trajectories. However, even after these curves are destroyed, their remnants may cause a stickiness effect which effectively traps chaotic trajectories thereby for a relatively long time. This can be also regarded as a (partial) shearless barrier. We have described those persistent barriers as the control parameter is varied.

The shearless barriers can also be investigated by altering the radial electric field profile, keeping constant the perturbation mode amplitude. This can be done in the context of our model by altering the position of the radial electric field extremum (k). As before, we can also detect the break-up and resurging of shearless barriers as the new control parameter is varied, and regions of barrier coexistence can be also observed. These multiple barriers can be related to double or triple shearless bifurcation. The effect of a small modification of the parameter k on the appearance of barriers could be validated in experiments for time-dependent electric fields.

In conclusion, varying the amplitude fluctuation or the electric shear, we find intervals of these control parameters for which the barriers onset and break-up are recurrent.

ACKNOWLEDGMENTS

The authors thank the financial support from the Brazilian Federal Agencies (CNPq), grants 407299/2018-1 and 302665/2017-0 and the São Paulo Research Foundation (FAPESP, Brazil) under grants 2018/03211-6, 2018/14435-2 and 2020/01399-8 and support from Coordenação de Aperfeiçoamento de Pessoal de Nível Superior (CAPES) under Grant Nos. 88881.143103/2017-01, Comité Français d'Evaluation de la Coopération Universitaire et Scientifique avec le Brésil (COFECUB) under Grant No. 40273QA-Ph908/18.

DATA AVAILABILITY

The data that support the findings of this study are available from the corresponding authors upon reasonable request.

[1] W. Horton, *Turbulent transport in magnetized plasmas*, 2nd ed. (World Scientific, 2018).

- [2] R. C. Wolf, *Plasma Physics and Controlled Fusion* **45**, R1 (2002).
- [3] R. D. Hazeltine and J. D. Meiss, *Plasma confinement* (Dover, 2003).
- [4] C. W. Horton Jr and S. Benkadda, *ITER Physics* (World Scientific, 2015).
- [5] R. J. Goldston, *Plasma Physics and Controlled Fusion* **26**, 87 (1984).
- [6] P. N. Yushmanov, T. Takizuka, K. S. Riedel, O. J. W. F. Kardaun, J. G. Cordey, S. M. Kaye, and D. E. Post, *Nuclear Fusion* **30**, 1999 (1990).
- [7] F. Wagner, G. Becker, K. Behringer, D. Campbell, A. Eberhagen, W. Engelhardt, G. Fussmann, O. Gehre, J. Gernhardt, G. v. Gierke, *et al.*, *Physical Review Letters* **49**, 1408 (1982).
- [8] J. W. Connor, T. Fukuda, X. Garbet, C. Gormezano, V. Mukhovatov, and M. Wakatani, *Nuclear fusion* **44**, R1 (2004).
- [9] X. Garbet, P. Mantica, C. Angioni, E. Asp, Y. Baranov, C. Bourdelle, R. Budny, F. Crisanti, G. Cordey, L. Garzotti, *et al.*, *Plasma Physics and Controlled Fusion* **46**, B557 (2004).
- [10] K. H. Burrell, *Physics of Plasmas* **4**, 1499 (1997).
- [11] I. L. Caldas, R. L. Viana, C. V. Abud, J. C. D. d. Fonseca, Z. d. O. Guimarães Filho, T. Kroetz, F. A. Marcus, A. B. Schelin, J. Szezech, D. L. Toufen, *et al.*, *Plasma Physics and Controlled Fusion* **54**, 124035 (2012).
- [12] F. M. Levinton, M. C. Zarnstorff, S. H. Batha, M. Bell, R. E. Bell, R. V. Budny, C. Bush, Z. Chang, E. Fredrickson, A. Janos, *et al.*, *Physical review letters* **75**, 4417 (1995).
- [13] E. J. Strait, L. L. Lao, M. E. Mauel, B. W. Rice, T. S. Taylor, K. H. Burrell, M.-S. Chu, E. A. Lazarus, T. H. Osborne, S. J. Thompson, *et al.*, *Physical review letters* **75**, 4421 (1995).
- [14] E. Mazzucato, S. H. Batha, M. Beer, M. Bell, R. E. Bell, R. V. Budny, C. Bush, T. S. Hahm, G. W. Hammett, F. M. Levinton, *et al.*, *Physical review letters* **77**, 3145 (1996).
- [15] P. J. Morrison, *Physics of Plasmas* **7**, 2279 (2000).
- [16] D. del Castillo-Negrete and P. J. Morrison, *Physics of Fluids A* **5**, 948 (1993).
- [17] D. del Castillo-Negrete, J. M. Greene, and P. J. Morrison, *Physica D* **91**, 1 (1996).
- [18] J. D. Szezech Jr, I. L. Caldas, S. R. Lopes, R. L. Viana, and P. J. Morrison, *Chaos* **19**, 043108 (2009).
- [19] I. C. Nascimento, Y. K. Kuznetsov, J. H. F. Severo, A. M. M. Fonseca, A. Elfimov, V. Bellintani, M. Machida, M. V. A. P. Heller, R. M. O. Galvão, E. K. Sanada, *et al.*, *Nuclear fusion* **45**, 796 (2005).
- [20] G. Van Oost, J. Adamek, V. Antoni, P. Balan, J. A. Boedo, P. Devynck, I. Duran, L. Eliseev, J. P. Gunn, M. Hron, *et al.*, *Plasma physics and controlled fusion* **45**, 621 (2003).
- [21] F. A. Marcus, M. Roberto, I. L. Caldas, K. C. Rosalem, and Y. Elskens, *Physics of Plasmas* **26**, 022302 (2019).
- [22] W. Horton, H.-B. Park, J.-M. Kwon, D. Strozzi, P. Morrison, and D.-I. Choi, *Physics of Plasmas* **5**, 3910 (1998).
- [23] F. A. Marcus, I. L. Caldas, Z. O. Guimarães-Filho, P. J. Morrison, W. Horton, Y. K. Kuznetsov, and I. C. Nascimento, *Physics of Plasmas* **15**, 112304 (2008).
- [24] R. M. Ferro and I. L. Caldas, *Physics Letters A* **382**, 1014 (2018).
- [25] K. W. Gentle, K. Liao, K. Lee, and W. L. Rowan, *Plasma Science and Technology* **12**, 391 (2010).
- [26] D. L. Toufen, Z. O. Guimarães-Filho, I. L. Caldas, F. A. Marcus, and K. W. Gentle, *Physics of Plasmas* **19**, 012307 (2012).
- [27] K. C. Rosalem, M. Roberto, and I. L. Caldas, *Nuclear Fusion* **54**, 064001 (2014).
- [28] F. Miskane, X. Garbet, A. Dezairi, and D. Saifaoui, *Physics of Plasmas* **7**, 4197 (2000).
- [29] K. C. Rosalem, M. Roberto, and I. L. Caldas, *Physics of Plasmas* **23**, 072504 (2016).
- [30] J. H. F. Severo, I. C. Nascimento, Y. K. Kuznetsov, R. M. O. Galvão, Z. O. Guimarães-Filho, F. O. Borges, O. C. Usuriaga, J. I. Elizondo, W. P. De Sá, E. K. Sanada, *et al.*, *Nuclear fusion* **49**, 115026 (2009).
- [31] C. G. L. Martins, R. E. de Carvalho, I. L. Caldas, and M. Roberto, *Journal of Physics A: Mathematical and Theoretical* **44**, 045102 (2010).
- [32] M. S. Santos, M. Mugnaine, J. D. Szezech, A. M. Batista, I. L. Caldas, and R. L. Viana, *Chaos* **29**, 043123 (2019).
- [33] J. D. Szezech Jr., I. L. Caldas, S. R. Lopes, P. J. Morrison, and R. L. Viana, *Physical Review E* **86**, 036206 (2012).